



HAL
open science

Relationship between microstructure, strength, and fracture in an Al-Zn-Mg electron beam weld: Part I: microstructure characterization

Quentin Puydt, Sylvain Flouriot, Sylvain Ringeval, Frédéric de Geuser, Guillaume Parry, Alexis Deschamps

► **To cite this version:**

Quentin Puydt, Sylvain Flouriot, Sylvain Ringeval, Frédéric de Geuser, Guillaume Parry, et al.. Relationship between microstructure, strength, and fracture in an Al-Zn-Mg electron beam weld: Part I: microstructure characterization. Metallurgical and Materials Transactions A, 2014, 45, pp.6129-6140. 10.1007/s11661-014-2566-9 . hal-01122459

HAL Id: hal-01122459

<https://hal.science/hal-01122459>

Submitted on 24 Apr 2023

HAL is a multi-disciplinary open access archive for the deposit and dissemination of scientific research documents, whether they are published or not. The documents may come from teaching and research institutions in France or abroad, or from public or private research centers.

L'archive ouverte pluridisciplinaire **HAL**, est destinée au dépôt et à la diffusion de documents scientifiques de niveau recherche, publiés ou non, émanant des établissements d'enseignement et de recherche français ou étrangers, des laboratoires publics ou privés.

Relationship Between Microstructure, Strength, and Fracture in an Al-Zn-Mg Electron Beam Weld: Part I: Microstructure Characterization

QUENTIN PUYDT, SYLVAIN FLOURIOT, SYLVAIN RINGEVAL,
FRÉDÉRIC DE GEUSER, GUILLAUME PARRY, and ALEXIS DESCHAMPS

This work presents a detailed, multiscale, spatially resolved study of the microstructure of an electron beam butt weld of the EN-AW 7020 (Al-Zn-Mg) alloy. Using a combination of optical, scanning and transmission electron microscopy, differential scanning calorimetry, and small-angle X-ray scattering, the distribution of phases in the different areas of the heat-affected zone and of the fusion zone is quantitatively characterized, for two different aging states: naturally aged after welding and artificially aged at 423 K (150 °C). The heat-affected zone consists of regions experiencing different levels of precipitate dissolution and coarsening during welding as well as new precipitation during post-welding heat treatment (PWHT). The microstructure of the fusion zone is typical from a fast solidification process, with a strong solute segregation in the interdendritic zones. The precipitate distribution after PWHT follows this solute distribution, and the resulting hardness is much lower than the relatively homogeneous value in the base metal and the heat-affected zone.

I. INTRODUCTION

PRECIPITATION hardening aluminum alloys are widely used in applications where specific strength is of strong importance, and particularly in all transportation sectors (automotive, aerospace, *etc.*). Their strength, plasticity, and fracture behavior are all closely related to the size and spatial distribution of nanometre-size precipitates. Many techniques exist for assembling such alloys.^[1] Although solid-state techniques such as friction stir welding appear very attractive to retain the potential for precipitation hardening in all the weld regions,^[2] in many cases it remains desirable or necessary to use fusion techniques, such as gas metal arc welding (GMAW), metal inert gas welding (MIG), laser beam welding (LBW), or electron beam welding (EBW). A review of these different techniques, applied on different alloys, can be found in Reference 3. During fusion welding, the solute is completely re-distributed by the solidification process and subsequent cooling to room

temperature. In adjacent zones (heat-affected zones HAZ), the material is subjected to a solid-state heat treatment that also completely disrupts the distribution of solute and related possibilities for nanoscale precipitation. The resulting mechanical properties of the assembly follow the heterogeneity of microstructure, and soft zones are generally encountered in the assembly of precipitation hardening alloys. The location of the softest zone (in the weld nugget or in the HAZ), as well as the severity of the strength loss, depend on many parameters such as the presence and nature of filler material, the type of welding process and process parameters, the nature of the alloy (*e.g.*, quench sensitivity) and geometry of the weld, or the application of a post-welding heat treatment. Moreover, a complete understanding of the mechanical properties of a weld assembly cannot be achieved simply by the characterization of the softest zone of the weld assembly. A detailed understanding of the spatial distribution of the microstructure and related mechanical properties is actually necessary, as the mechanical behavior during plasticity (and particularly the stress state) depends on the interplay between the sample geometry and the distribution of soft and hard zones along the weld joint.^[4]

The EN-AW-7020 aluminum alloy (subsequently named 7020 in this paper) is a medium strength alloy particularly suited for welding.^[5,6] The good weldability of this alloy results from several features: (i) very low quench sensitivity^[7]; (ii) hardening during natural or artificial aging; and (iii) very low content of copper (at impurity level) which helps avoiding hot cracking phenomena during solidification of the weld pool.^[8] EBW presents advantages compared to other welding

QUENTIN PUYDT, formerly Ph.D. Student with the SIMAP Laboratory, Université Grenoble Alpes, 38000 Grenoble, France, also with the CNRS, SIMAP, 38000 Grenoble, France, and also with the CEA Valduc, 21120 Is-Sur-Tille, France, is now Research Scientist with the IRT M2P, Metz, France. SYLVAIN FLOURIOT and SYLVAIN RINGEVAL, Research Scientists, are with the CEA Valduc. FRÉDÉRIC DE GEUSER, Research Scientist, is with the SIMAP Laboratory, Université Grenoble Alpes, and also with the CNRS, SIMAP. GUILLAUME PARRY, Associate Professor, and ALEXIS DESCHAMPS, Professor, are with the SIMAP Laboratory, Université Grenoble Alpes, also with the CNRS, SIMAP, and also with the Grenoble Institute of Technology, Grenoble, France. Contact e-mail: alexis.deschamps@grenoble-inp.fr

processes.^[9,10] The high energy density permits a large penetration depth with high depth-to-width ratio. In addition, high welding velocities are achievable, reducing the extension of the HAZ. Welding is performed in a high vacuum chamber, limiting the extent of molten metal oxidation and other contamination *e.g.*, by moisture.

Nevertheless, EBW leads to significant microstructural evolutions that impact the properties of the base metal (BM).^[11–13] In particular, the evaporation of some alloying elements, observed in high density energy processes, is a concern.^[14,15] This phenomenon changes the local chemical composition and therefore affects the mechanical properties and the fine scale precipitation potential of the alloy even when a solution treatment is applied after the welding process.^[15]

The precipitation sequence in medium strength Al-Zn-Mg alloys involves three main precipitate types.^[16–19] At room temperature, GP zones are observed to form subsequently to the solution treatment; during higher temperature heat treatments, they are replaced by the metastable precipitate η' , which offers the highest strength to the alloy, and eventually by the equilibrium phase η .^[20] These precipitates are generally homogeneously distributed inside the grains. Yet some microscopic heterogeneities of precipitation distribution exist, such as the precipitate-free zone (PFZ) along the grain boundaries, which affect the damage and fracture properties.^[21,22] Moreover, at the grain boundaries and dispersoid particles, coarse η precipitates are nucleated when the quench from the solution treatment is imperfect.^[7] In the fusion zone of 7020 welds, the distribution of solute elements is spatially heterogeneous and the microstructure consists of insoluble impurity-containing particles, solute-rich and solute-poor regions linked to the solidification history.^[14,15]

In a series of two papers, we aim at establishing a microstructure-based mechanical model capable of describing quantitatively the plastic behavior until ductile fracture of this 7020 alloy lap joined by EBW with no filler material. The present paper will be devoted to the detailed description of the weld microstructure. The microstructure study will be both multiscale (from the scale of the grains down to that of the precipitates) and spatially resolved across the different weld zones. It will serve as a basis for the mechanical model that will be presented in the companion paper.^[23]

The study of microstructures in fusion welded precipitation hardening aluminum alloys is a well-chartered area. Particularly, the evolution of precipitate microstructures in the HAZ during welding and during post-welding heat treatments is now well understood both in terms of characterization and modeling in the most important Al alloy families and in particular in Al-Mg-Si based alloys^[24–26] and in medium strength Al-Zn-Mg alloys.^[27–29] What happens in the fusion zone has attracted more limited attention. There the phenomena are complex, since the distribution of solute becomes heterogeneous at the scale of the solidification microstructure, and some mixing with the filler material may completely change the alloy composition. However, it is recognized that appropriate welding conditions and

post-welding heat treatments can result in significant nanoscale precipitation within the weld nugget and associated hardness recovery.^[30–33]

In the present work, no solution treatment is applied subsequently to the welding process. As a result, the alloying elements are heterogeneously distributed within the microstructure of the fusion zone (FZ). In order to investigate the effect of a post-welding heat treatment, two different microstructures are generated: one after a natural aging (NA state) and the other after a combination of natural and artificial aging (AA state). The microstructure is studied using a wide range of complementary techniques at different scales: optical, scanning electron and transmission electron microscopy (OM, SEM and TEM), differential scanning calorimetry (DSC), small-angle X-ray scattering (SAXS), and microhardness for relating the microstructure to the spatial distribution of strength.

II. MATERIALS AND EXPERIMENTAL METHODS

A. Base Metal (BM)

The chemical composition of the alloy used in this study is (in wt pct) 4.65 pct Zn, 1.25 pct Mg, 0.02 pct Cu, 0.11 pct Mn, 0.28 pct Cr, 0.09 pct Fe, 0.04 pct Si, 0.13 pct Zr, and 0.04 pct Ti. The alloy was received as a forged bar in a peak aged T652 temper. Prior to welding, the BM presents a fibrous structure as illustrated in Figure 1 (the micrographs are obtained after orthophosphorous acid etching). In this representation, the longitudinal direction (L) of the forging and the transverse directions (T) is identified.

B. Welding and Heat Treatment

Plates of 7 mm in thickness and $10 \times 5 \text{ cm}^2$ in size were machined from the base metal, so that the forging direction was the short transverse direction of the plate. These plates were butt welded in an Alcatel[®] high vacuum equipment, with energy per unit of length equal to 150 kJ m^{-1} . Once assembled, the welded plates formed a unique plate of $10 \times 10 \text{ cm}^2$. The depth of penetration of the weld was comprised between 5 and 5.5 mm.

After welding, two states of aging were characterized: one resulted of 15 days of natural aging and will be named naturally aged or NA state; the other was obtained after 15 days of natural aging followed by 48 hours at 423 K (150 °C) (ramp heating 80 K h^{-1}) and will be named artificially aged or AA state.

C. Methods

In order to evaluate the loss of solute elements in the fusion zone, concentrations profiles were measured using electron probe microanalysis (EPMA). Measurements dispersion due the segregation of alloying elements was avoided by subjecting the samples used for that purpose to a full solution treatment at 738 K (465 °C) for 35 minutes.

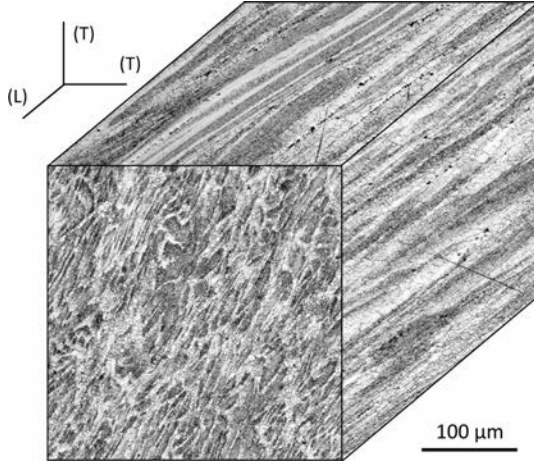


Fig. 1—3D reconstruction from optical micrographs of the grain structure of the base metal.

Scanning electron microscopy in backscattered electrons detection mode (SEM-BSE) was used on polished samples to reveal the iron-based intermetallic particles distribution, and to evidence the segregation of zinc in the solidification microstructure.

The heterogeneities of hardening precipitate distribution, precipitates at grain boundaries, and nature of coarse intermetallic particles were studied by TEM. Specimens were prepared by sectioning, mechanical polishing down to 100 μm , and electropolishing in a solution containing 1/3 nitric acid and 2/3 methanol operating at 253 K under 15 V. Samples were observed in a Jeol 3010 microscope at 300 kV. Most of the images shown in the results section were deliberately taken far from any zone axis in order to have a uniform (yet weak) contrast for the precipitate distribution, making it easier to identify the heterogeneities of the precipitate distribution. The higher magnification, more contrasted bright field micrographs, were taken close to a [110] zone axis.

DSC was used to characterize the nature of precipitates. The samples, of size about $1 \times 1 \times 1.5 \text{ mm}^3$, were machined in different zones of the weld. A fast heating rate of 150 K min^{-1} from 223 K to 738 K ($-50 \text{ }^\circ\text{C}$ to $465 \text{ }^\circ\text{C}$) was used in order to minimize the transformation of metastable phases into more stable ones during the heating operation. In that way the position of the dissolution peaks of the phases initially present in the sample could be unambiguously identified.

SAXS is a common technique for measuring size and volume fraction of hardening precipitates^[34,35] in the nanometre-size range. The samples consisted of thin foils about 70 μm in thickness. Most measurements presented here were carried on a laboratory set-up using a rotating anode at the Cu K α wavelength and a CCD detector, with a beam of $1 \times 1 \text{ mm}^2$; maps of the precipitate distribution were obtained at the European synchrotron radiation facility ESRF, on the BM02-D2AM beam line, where the beam size was about 200 μm in diameter. All data were corrected for elec-

tronic noise, detector efficiency, and background noise subtraction. The data were normalized using a glassy carbon standard.^[36]

The precipitate size was calculated from the X-ray diffraction spectra by assuming that the precipitate size distribution followed a lognormal distribution of spheres, which is the most common assumption for describing precipitate microstructures^[37]:

$$f(R) = \frac{1}{\sigma R_m \sqrt{2\pi}} \exp\left\{-\frac{1}{2} \left[\frac{\ln(R/R_m)}{\sigma}\right]^2\right\}, \quad [1]$$

where R_m is the median radius and σ the dispersion parameter. From these parameters, the mean radius of the distribution was determined by using the formula $R_{\text{mean}} = R_m \exp\left(\frac{\sigma^2}{2}\right)$. These parameters were extracted by fitting the experimental curves to the intensity predicted from this precipitate size distribution, see.^[34] This method was extended for two coexisting distributions when necessary (such as GP zones and η' precipitates, which exhibit significantly different sizes). The dispersion parameter was found to be about 30 pct in all conditions.

The precipitate volume fraction was calculated from the value of integrated intensity, calculated as described in References 34:

$$Q_0 = \int_0^\infty I(q)q^2 dq = 2\pi^2(\rho_p - \rho_m)^2 f_v(1 - f_v) \quad [2]$$

In this expression, ρ_p and ρ_m are, respectively, the electron density in the precipitate and in the matrix, which are calculated from the concentration of each species. The aluminum matrix was considered fully composed of aluminum. As it is very complex to give an exact composition for each type of precipitates (especially for metastable forms, whose composition can vary depending on the microstructural state, see for example^[38]), we considered for simplicity the following precipitate compositions:

- Zn/(Mg + Al) = 1 for the GP zones
- Zn/(Mg + Al) = 1.5 for the η' precipitates
- Zn/(Mg + Al) = 2 for the η precipitates

III. RESULTS

A. Grain Structure and Solute Content Distribution

Figure 2 is a micrograph of the weld composed of a montage of optical micrographs in dark field mode. The smooth shape of the FZ appears clearly, with a penetration depth of about 5 mm and a depth-to-width ratio close to 1.

This mode of imaging highlights the grain structure. Outside the FZ, the metal exhibits a vertical fibrous orientation. In the FZ, the grains are refined and mainly isotropic. Their size is significantly different depending on their location: they are very refined on the edges (a few μm) and larger at the center (of the order of 100 μm), close to the free surface. These differences in

size could be explained by higher cooling rate during solidification close to the internal edges, where the base material serves as a heat sink.

Solute concentration profiles, measured by EPMA at three different depths in the welded plate (as represented by arrows on Figure 2), are presented in Figure 3. The FZ experiences a significant loss of zinc and magnesium. The concentration of the other elements in the alloy remains constant. These profiles show that the loss is roughly constant in the depth of the FZ. An average on the values in the FZ for each element gives a loss of 33 pct of zinc and 18 pct in magnesium.

B. Particle Distribution: SEM Observations

Figure 4(a) shows the limit between the un-melted metal and the FZ. The white phases present in the BM are iron-based intermetallic particles (as confirmed by EDX measurements). The crystallographic contrast makes it also possible to identify the grain structure and the sharp transition with the fusion zone. The FZ side presents a much finer grain structure, with a cell size of the solidification structure typically between 5 and 10 μm (see Figure 4(b)); in addition, the cell structure is delineated by a diffuse chemical contrast. EDX analysis shows that the light areas contain a higher Zn content than the cell centers, in accordance with the fact that they correspond to the end of the solidification process. Due to this heterogeneous distribution of the precipi-

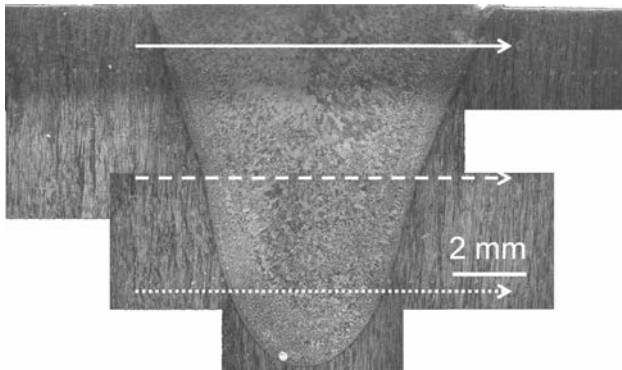


Fig. 2—Optical micrograph of the weld—dark field mode.

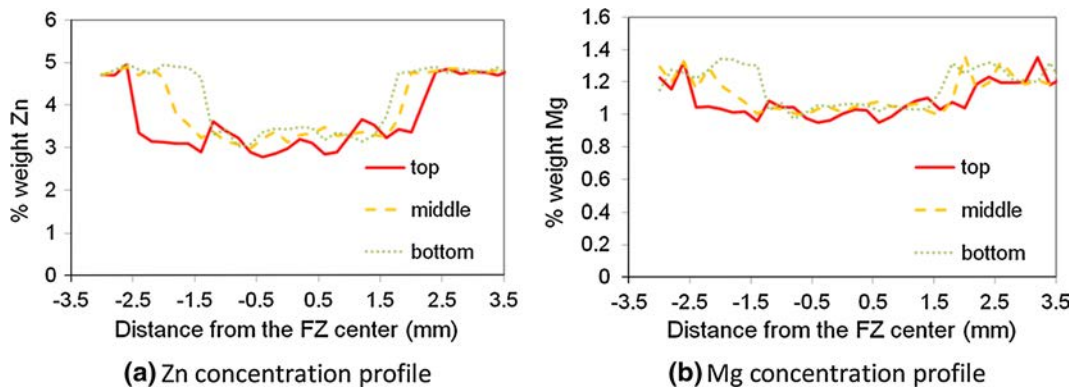


Fig. 3—Concentration profiles of Zn and Mg elements along the weld.

tate-forming solutes, it can be expected that the distribution of hardening precipitates after aging will also be heterogeneous, which will be confirmed further below by TEM observations. In conjunction to these diffuse light areas, small sub-micron size spherical white particles are observed, mainly lying on grain boundaries. These particles are identified by EDX as iron-based intermetallic particles. At this scale, no differences were observed between the NA and AA states.

C. Precipitate Distribution: TEM Observations

The distribution of strengthening precipitates in the different weld zones will now be presented. Figure 5 shows two micrographs at low and higher resolution of the BM in the T652 temper. The microstructure consists of a relatively homogeneous distribution of nanoscale precipitates, identified as η' precipitates by selected area diffraction. The larger quench-induced equilibrium η precipitates that are observed to form on the dispersoids and grain boundaries certainly originate from the quench preceding the T652 temper. Figure 6 shows the microstructure when the BM was subjected to the post-welding heat treatment (48 hours at 423 K). Qualitatively in the TEM, no modification of the microstructure can be observed, with the same characteristic features. This heat treatment certainly induces some precipitate growth and/or coarsening that will be investigated by more suitable experimental techniques.

After welding and natural aging of 15 days, all the initial precipitates have disappeared in the FZ (Figure 7(a)). GP zones may be present in this condition but they are difficult to observe in the TEM and their presence will be assessed by SAXS and DSC later in the paper. The lack of coarse precipitation at the grain boundaries highlights the fast cooling rate undergone by the FZ after solidification. The cooling and associated internal stresses also induce some plastic deformation as shown by the presence of dislocations. After the post-welding heat treatment leading to the AA state, fine scale precipitates are observed in the FZ (Figure 7(b)), as well as coarser precipitates at the grain boundaries (however still of a smaller size and density compared to the heat-treated BM). The fine scale precipitation is mostly of η' -type. The most striking observation in the

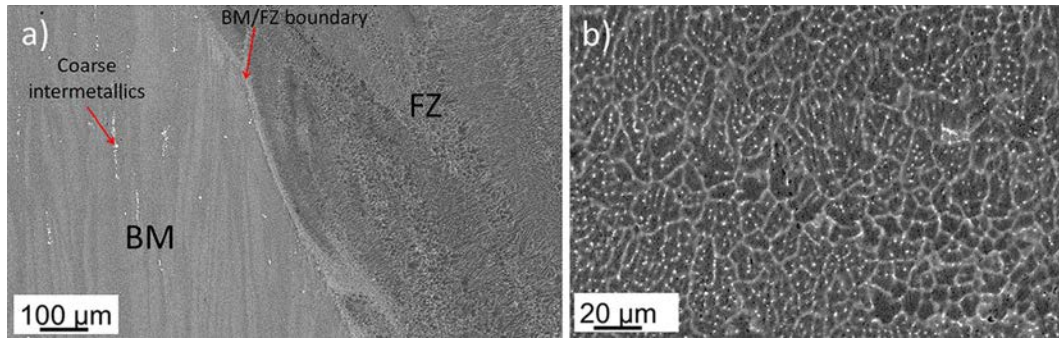


Fig. 4—SEM-BSE micrographs (a) of the weld-based metal interface and (b) of the weld nugget.

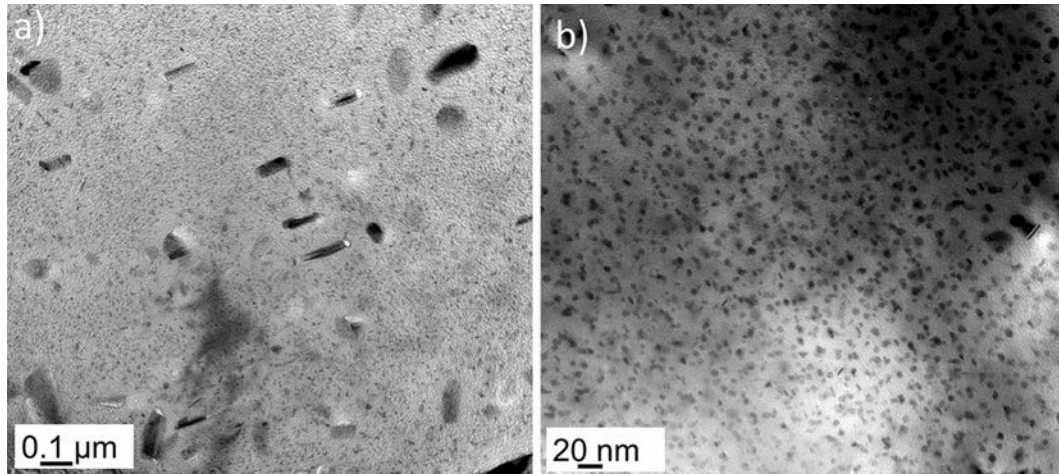


Fig. 5—TEM micrographs of the base metal in the T652 temper.

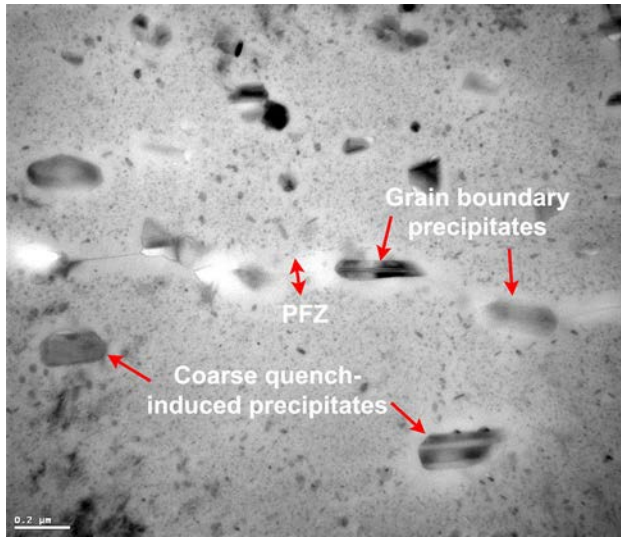


Fig. 6—Typical TEM micrograph of the base metal in the T652 + 48 h at 150 °C state.

FZ is that the fine scale precipitation is heterogeneously distributed. On the top right corner of Figure 7(b), the distribution of η' is similar to that of the BM in the T652 temper. On the bottom left, however, the material is entirely void of precipitates, due to the segregation of

the main solute elements as evidenced by the SEM observations.

At the core of the solute-rich (and consequently precipitate-rich) areas, one finds the intermetallic iron-based particles (see Figure 8), which were observed in the SEM. These particles are actually composed of a loosely coherent multitude of nanocrystals. One can tentatively relate the very small crystallite size of these particles to the fast solidification rate experienced in the fusion zone and the lack of coherency of these particles clusters to the volume loss at the end of solidification that these zones need to accommodate.

Concerning now the HAZ, Figure 9(a) shows the microstructure after natural aging, 5 mm from the fusion zone (distance from the center of the FZ) and Figure 9(b) 6 mm from the fusion zone. At 5 mm from the fusion zone, almost no precipitates are observed, including on the grain boundaries, meaning that even the coarse precipitates present initially have been dissolved during welding. At 6 mm from the fusion zone, however, the coarse precipitate distribution resembles that of the base material. Yet no fine precipitates are found, meaning that the temperature spike was sufficient to dissolve most of the small hardening precipitates but not the coarse quench-induced ones.

After the post-welding heat treatment, homogeneous hardening precipitation appears in the HAZ, as well as some coarser precipitates at the grain boundaries, which

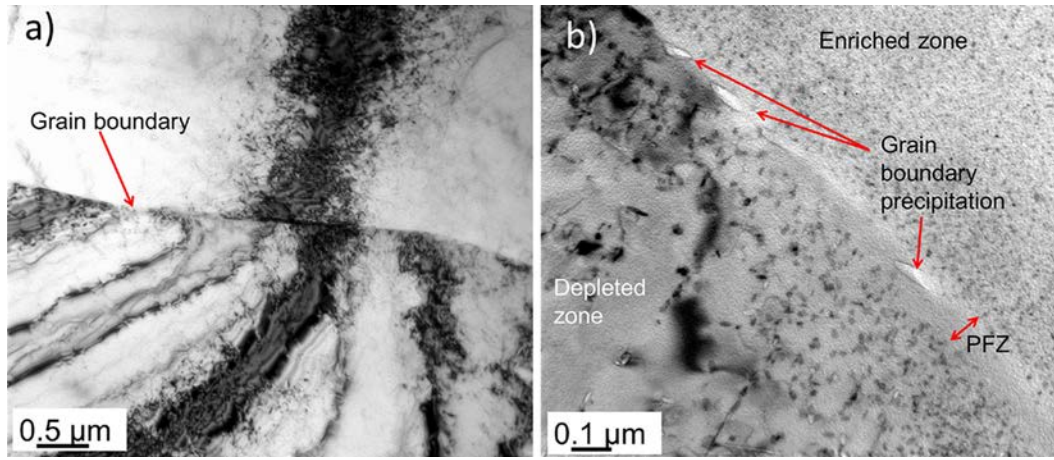


Fig. 7—TEM micrographs of the fusion zones (a) in the NA state and (b) in the AA state.

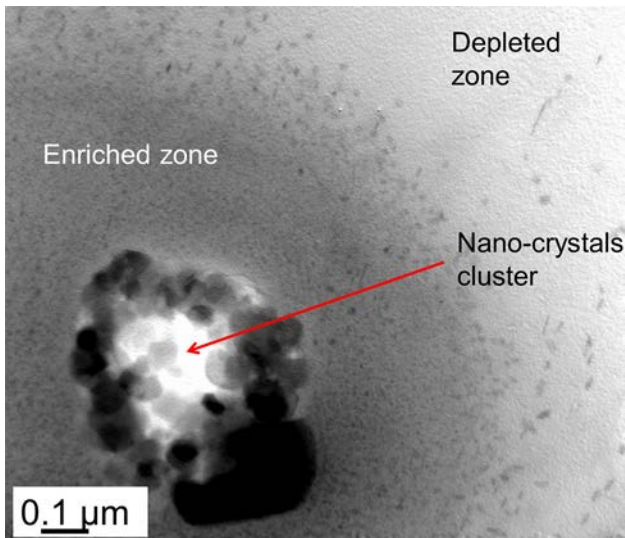


Fig. 8—TEM observation of an iron intermetallic particle cluster in the fusion zone, AA state.

leads to a microstructure very close to that observed for the BM, but with a lower proportion of coarse precipitates (see Figure 10).

D. Characterization by DSC and SAXS of the Precipitates in Characteristic Locations

The TEM observations presented above provide a qualitative view of the precipitation processes encountered in the different areas of the welded plates, both in the NA and in the AA states. In order to characterize more precisely the type of precipitates formed and their size, we have carried out in parallel DSC and SAXS measurements.

Figure 11 displays the Kratky plots of the SAXS intensity and the DSC thermograms obtained at some representative positions of the weld. These positions are the FZ, the BM, and two intermediate locations in the HAZ: 4 and 6 mm from the center of the FZ. In the

Kratky plot, a peak corresponds to a given precipitate size distribution. Its position is inversely proportional to the precipitate size and its area is proportional to the precipitate volume fraction. The η' precipitates present in the BM (T652 temper) have an average radius of about 2 nm. To this precipitate type and radius is associated a well-defined sharp dissolution peak during the DSC scan at approximately 523 K (250 °C), confirming that in this temper the majority of precipitates are of the same nature.

The Kratky plots obtained in the FZ and HAZ1 show a broad peak located at higher values of scattering vector q , typical of the presence of GP zones (radius between 0.7 and 0.8 nm). The thermograms validate this interpretation with a dissolution peak at much lower temperature [423 K (150 °C)] as compared to that of the η' phase in the BM. These GP zones can have appeared during the last stages of cooling after welding and during the 15 days of subsequent natural aging. An important observation is that their size and their dissolution temperature are both very similar in the FZ and HAZ1, despite the difference in overall solute content and more importantly the difference in the distribution of solute. However, consistently with the lower solute content present in the FZ, this location shows a lower fraction of GP zones as evidenced both by the DSC curve area and by the area under the Kratky plot.

In the HAZ2, both GP zones and η' coexist, as evidenced by the presence of two peaks in the Kratky plots and in the DSC scans. This zone corresponds to the micrograph shown on Figure 9(b): the smallest precipitates have been dissolved, but a fraction of large ones are still there. The peak corresponding to the large precipitates in the Kratky plot is located at smaller scattering vectors as compared to that of the BM, consistently with a larger average value of the precipitate size, and with a shift to higher temperatures of the DSC dissolution peak.

The thermograms obtained after post-welding heat treatment (PWHT) for the different zones are plotted in Figure 12(b). The thermal treatment [48 hours at 423 K (150 °C)] on the BM initially in the T652 state results in

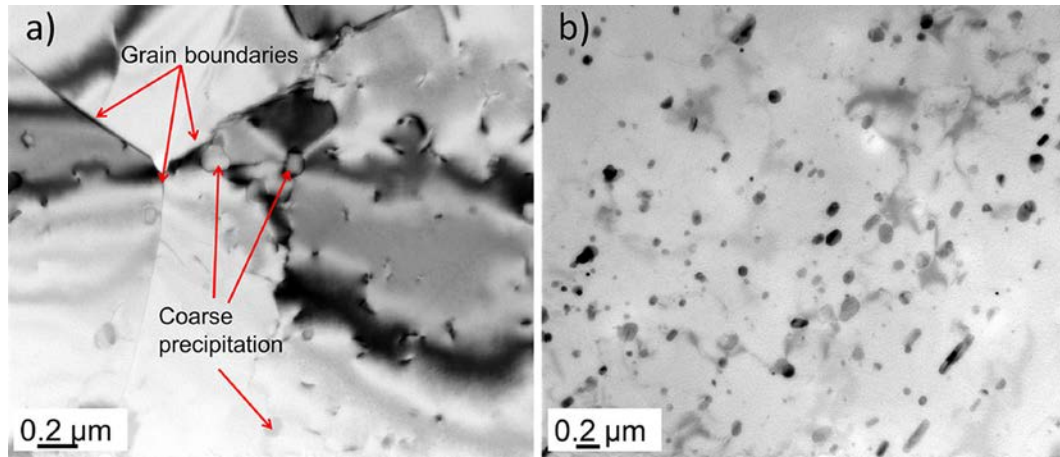


Fig. 9—TEM micrographs in the heat-affected zone (a) 5 mm from the center of the fusion zone and (b) 6 mm from the center of the fusion zone (NA state).

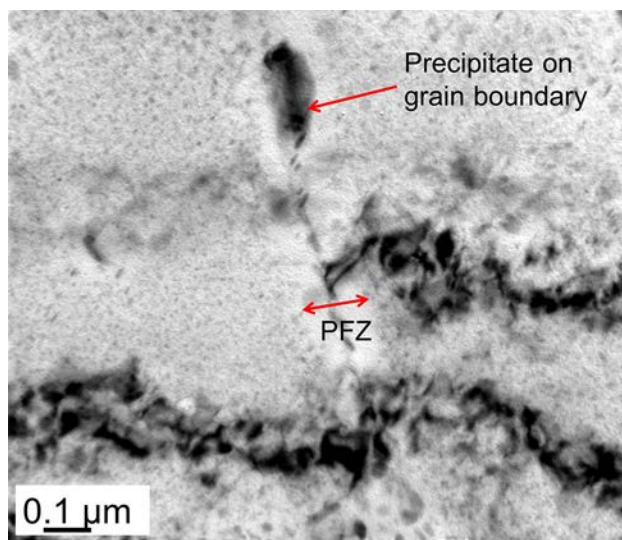


Fig. 10—TEM micrograph in the heat-affected zone (AA state).

a significant over-aging of the precipitate microstructure: part of the dissolution peak remains at the same temperature, while a shoulder appears, which can be attributed to the transformation of the η' precipitates into more stable η phase. The peaks of both HAZ (1 and 2) are quite similar, showing a homogenization of the microstructure across the HAZ due to the PWHT. Their dissolution peak is intermediate between that of the BM and that of the artificially aged BM. The thermogram of the FZ, however, is very different from the others. In terms of precipitate type, it is characteristic of an over-aged temper (quite similar to the PWHT BM) but the peak area clearly shows a lower volume fraction, which is clearly related to the lower solute content.

E. Spatially Resolved Precipitate Characterization and Related Hardness Profiles

In order to resolve spatially the distribution of precipitates along the weld in the NA and AA states,

we carried out small-angle X-ray scattering measurements along lines at mid-thickness of the welded plate, with a scan step of 0.5 mm (meaning that some smearing of data is unavoidable here because the beam size is of the order of 1 mm). The profiles of precipitate size, precipitate volume fraction, and related hardness measured in the same locations are shown in Figure 13. For the naturally aged weld, we differentiate between the GP zones and η'/η precipitates by their respective size (radius smaller than 1 nm for the former and larger than 1.5 nm for the latter). In some locations of the HAZ, the two phases are present simultaneously and their contributions are separated. Depending on the evolution of precipitate size and volume fraction, we define several sub-sets of the HAZ as defined in the figure, whose characteristics will be detailed below.

1. NA state

Before the artificial aging treatment, the FZ and HAZ1 contain exclusively GP zones: the temperature reached during welding in these zones has been high enough to dissolve the precipitates initially present; following welding the matrix is then a supersaturated solid solution and GP zones are formed during aging at room temperature. The size of GP zones formed in the FZ and HAZ1 is very similar, although slightly smaller in the FZ. The volume fraction is, however, very different as already discussed above. The HAZ1 contains twice the volume fraction as compared to the FZ, and this volume fraction appears homogeneous in these respective areas, with a sharp transition between them.

The HAZ2 is the zone where the dissolution of the initially present precipitates is incomplete, and where the resulting super saturation is large enough after welding to induce some GP zones formation. In this region, the remaining η'/η precipitates have an average size much larger than that of the BM, as has been already observed in other types of welds before.^[29] Further away from the weld center, the last heat-affected zone is HAZ3, where the dissolution of η' precipitates is partial, and the super saturation resulting from the welding operation is not sufficient to enable the formation of GP zones during

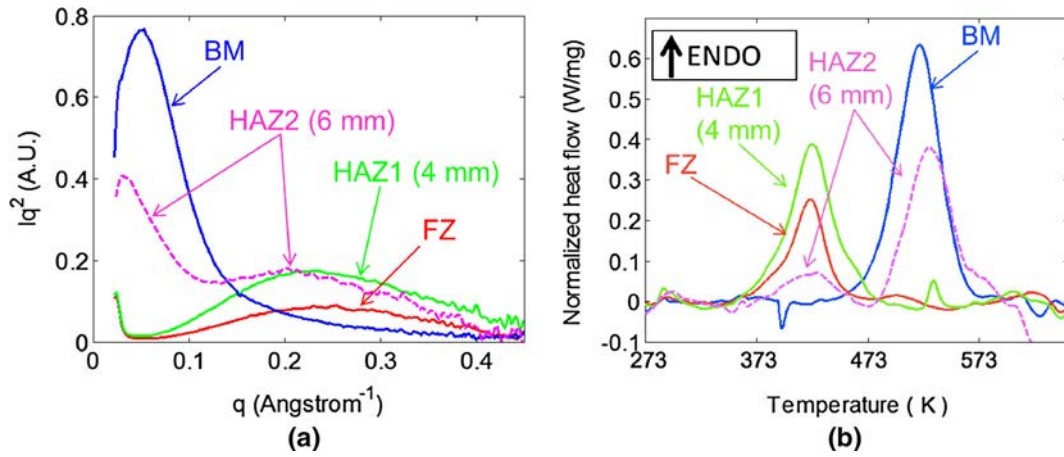


Fig. 11—SAXS Kratky plots (a) and DSC thermograms (b) for different zones of the weld (NA state).

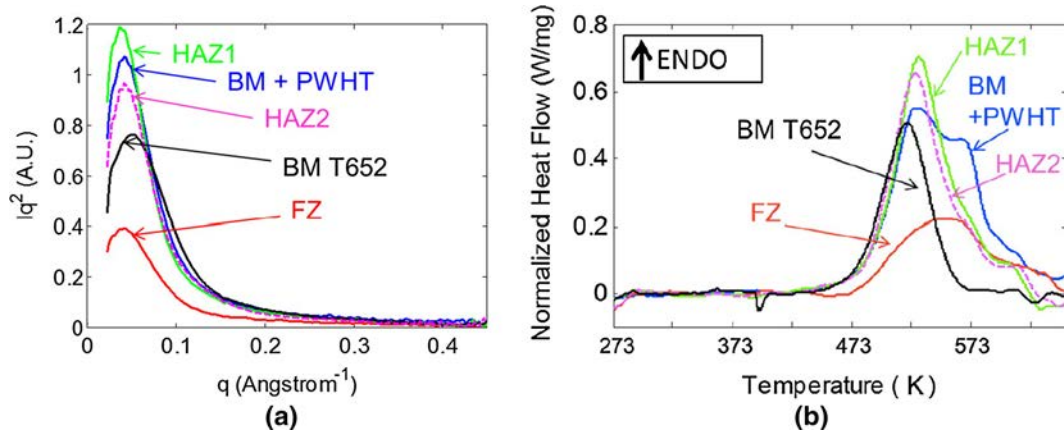


Fig. 12—DSC thermograms for different zones of the weld (AA state).

room temperature aging. In these stages of moderate dissolution of the precipitates, their average size is observed to remain approximately constant, as has been observed in similar conditions before^[29] and explained by modeling.^[28]

In terms of hardness, it is possible to identify three main zones. The softest zone is the FZ, where the low volume fraction of GP zones formed after welding is not compensated by the finer grain size. This zone has a hardness of about 70 HV as compared to 120 HV for the base material. The HAZ1 and HAZ2 have a relatively homogeneous hardness of about 110 HV, which is only slightly lower than the hardness of the BM, showing that the formation of GP zones provides a very good hardening increment. In HAZ3, the hardness is observed to progressively reach the hardness of the base metal. A slight hardness dip is found at the border between HAZ2 and HAZ3, where the dissolution of η' precipitates is significant and yet formation of GP zones is still not possible.

2. AA state

After the heat treatment, precipitates are only of η'/η -type. They show a relatively constant mean radius along

the measurement line. Nevertheless, the mean size is slightly larger in the FZ and in the outside edge of HAZ2. In the FZ, this is consistent with the slightly over-aged state detected by DSC measurements. In the HAZ2, the slightly larger average size reflects the larger size of the precipitates that were present at the end of the welding operation. The fact that the average size in this region has decreased during the PWHT means that new precipitates have nucleated, whereas another mechanism could have happened, namely the diffusion of free solute to the precipitates already present before the PWHT.

Concerning the volume fraction, it is observed to be relatively homogeneous as well, except of course in the FZ where the lower solute content and the heterogeneous distribution of solute result in a very low volume fraction.

In terms of hardness distribution, the relatively homogeneous size and volume fraction of the precipitates throughout the HAZ translate into a homogeneous hardness distribution, with only a slight dip in the HAZ2 where the precipitate size shows signs of over-aging. In the FZ, however, the hardness is much lower, and remains comparable to the hardness in the NA state.

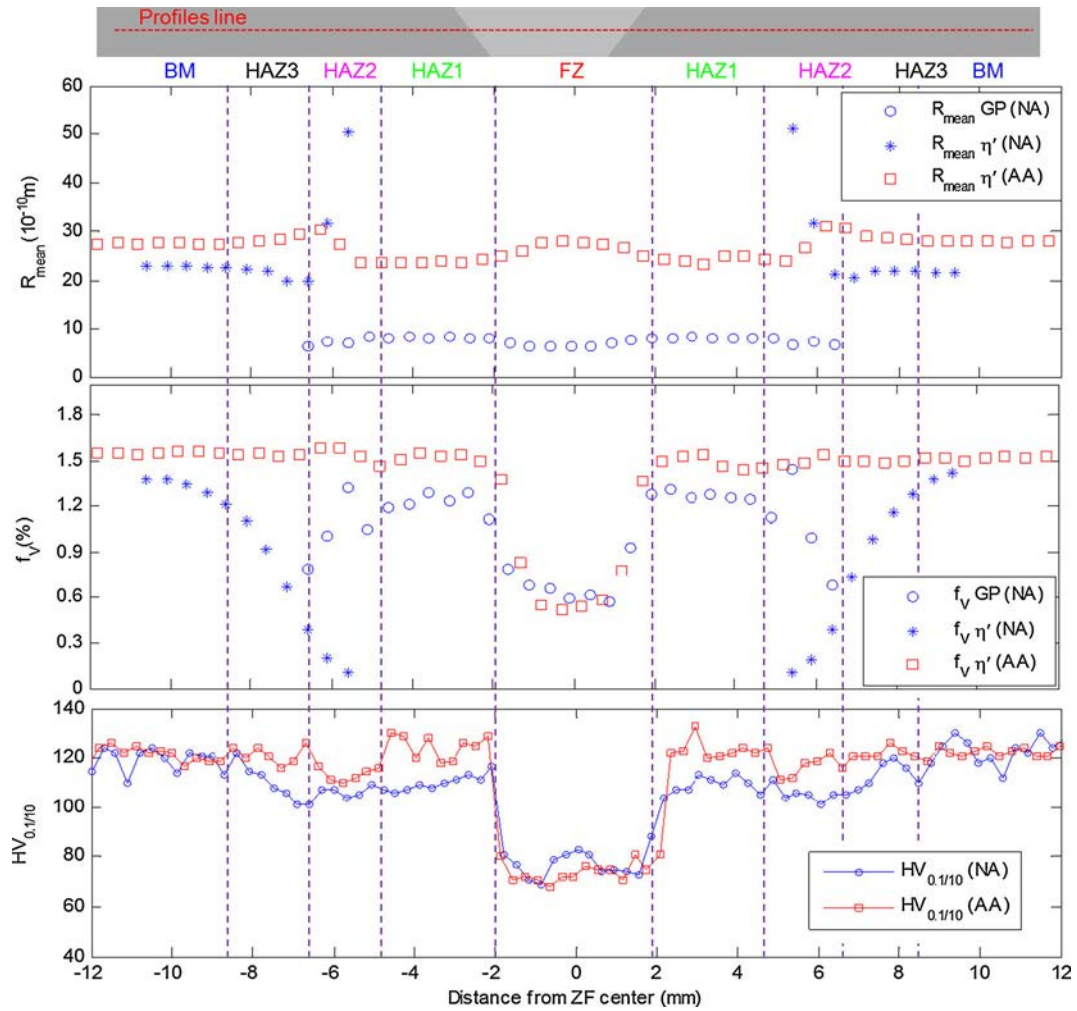


Fig. 13—Mean radius R_{mean} (top), volume fraction (middle), and microhardness HV (bottom) along the weld for both NA and AA states.

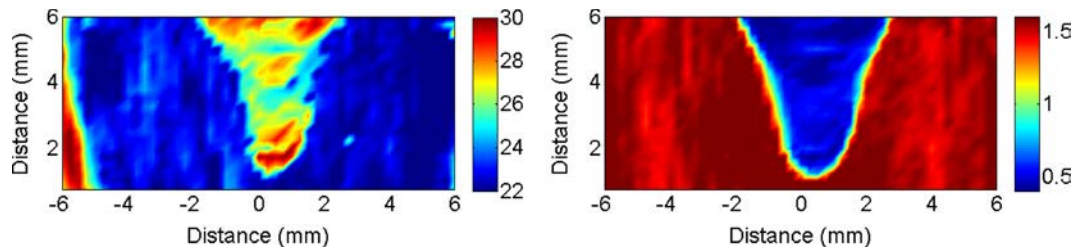


Fig. 14—Maps of mean radius (left) in Angströms and volume fraction (right) in pct.

The spatial distribution of precipitate microstructures described above provides a satisfactory description along one line across the weld. However, some questions remain about the spatial distribution of precipitate states through the plate thickness; namely, about the shape of the iso-precipitation profiles as compared to the shape of the weld pool, and about the possible heterogeneity of precipitate states within the different regions of the FZ and HAZ. In order to provide answers to these questions, a thin foil (about 70- μm thickness) of the weld in the AA state, normal to the welding direction, was scanned by a synchrotron X-ray beam

and SAXS measurements were performed with a scan step of 250 μm in both directions (which is slightly larger than the beam size of 200 μm). The resulting microstructure maps (precipitate radius and volume fraction) are shown in Figure 14. The main features of the line scans are of course confirmed by these measurements, namely a relatively homogeneous distribution of precipitate size and volume fraction in the HAZ, a larger precipitate size in the FZ, and a much lower precipitate volume fraction in the FZ. The 2D nature of the measurements shows that no significant variation of microstructure is present through the thickness of the

plate. This is particularly true not only in the HAZ, but also in first approximation in the FZ, where the precipitate size and volume fractions are observed to be rather homogeneous. This homogeneity is consistent with the homogeneity of solute content determined by EPMA at three different depths in the plate.

It should be emphasized that the explored region does not permit to see the entire HAZ: the larger mean radius on the extreme left of the map corresponds to the beginning of HAZ2, where these measurements confirm that the average particle size has a larger value.

IV. DISCUSSION

The results presented above draw a clear picture of the evolution of precipitate microstructures across the weld during and after welding. Some of the features are those classically observed in most welding processes, and some others are rather specific to the EBW technique.

The distribution of precipitate microstructures in the different regions of the heat-affected zone has been the subject of several studies before, with different applied welding techniques. A few studies only have provided a spatially resolved characterization of the microstructure in the different regions of the weld and HAZ^[15,29,39-42], in most other studies, only the distribution of hardness across the weld has been used as a probe for microstructural variation; however, a good insight can already be obtained in this way. The welding process results in a heat spike in the HAZ, whose peak temperature depends on the distance to the weld center. The relationship between this distance and the peak temperature obviously depends on numerous parameters (welding technology, welding parameters, plate dimensions, heat transfer,...); however, in a fusion process all peak temperatures up to the fusion temperature are necessarily present in the HAZ. Nevertheless, the detailed shape of the temperature spike depends strongly on the above-mentioned parameters, and it can be expected that the behavior of precipitates submitted to this kind of temperature history depends not only on the peak temperature but also on the heating rates and cooling rates before and after this peak. When precipitates are present in the microstructure before welding, it is classically found that the HAZ can be divided in several sub-zones. In the zone closest from the BM (what we have called HAZ3), the precipitates start to dissolve first at constant radius, *i.e.*, the volume fraction decreases when the distance to the weld center decreases, whereas the average precipitate radius remains constant. Modeling has helped to understand that this constant radius results from the combination of the fast disappearance of small precipitates into the solid solution and slow evolution of the more stable large precipitates of the precipitate size distribution (PSD).^[28] Closer to the weld center, one finds a zone where the precipitates coarsen, and their volume fraction is very small. This behavior is again typical of the last stages of precipitate reversion and it can be quantitatively predicted by precipitation modeling

when the thermal profiles are available.^[43] In a third zone very close to the weld center, precipitates are completely dissolved and new low temperature phases such as GP zones can form during natural aging.

During artificial aging, this set of microstructures evolves further due to precipitate formation in the regions where the initial precipitates had dissolved, and coarsening where they were not affected. In this sense, the behavior observed in the present study is also typical of what has been reported in similar alloys before.^[4,29] However, what happens in the zone of incomplete precipitate dissolution is more complex, since it depends on the possibility to nucleate new phases along the ones that have survived reversion. Therefore, a variety of behaviors can be found during PWHT in this zone, and quite often it is found that it is the softest one due to a lack of precipitate nucleation and extensive growth of the surviving precipitates from the solid solution released during reversion. In the present case, however, such behavior is not observed. The precipitate size after PWHT is relatively homogeneous with only a moderate over-aging, and the resulting distribution of hardness is homogeneous as well. It has been shown before that during the last stages of reversion, the extent of the increase of the precipitate size was more pronounced when the heating rate was decreased.^[44] Thus, it is likely that this lack of pronounced coarsening and hardness dip in the HAZ2 is linked to the very high heating and cooling rates encountered in the EBW process as compared to other types of welding techniques investigated in similar studies before (such as MIG welding in Reference 29).

Another specific feature evidenced in the present study is the particular precipitate distribution in the fusion zone. In relation with the high cooling rate during solidification of the weld pool, it can be postulated that diffusion in the forming solid phase is negligible. In such solidification conditions (Scheil-Gulliver), high solute gradients are generated, and the eutectic forming solutes segregate to the regions that solidify last, as was evidenced by BSE-SEM observations. During subsequent aging treatments, diffusion is restricted to small distances and therefore homogenization of the solute distribution does not occur contrarily to what was observed when a post-welding solution treatment was applied.^[15] Thus, depending on the moment at which a given zone has solidified, it will act during precipitation as an alloy of different solute contents, and the resulting precipitate distribution is highly heterogeneous. The interdendritic regions show a very high precipitate density, which may actually be substantially higher than in the base material because their solute content is the highest solubility of the single phase Aluminum domain. In contrast, the dendrite cores, of low solute content, are completely precipitate free. At the boundary between these two regions, the solute content gradually changes and the precipitation process becomes progressively more difficult, resulting in a lower precipitate density and a larger size. As a result, the average precipitate size measured in the FZ is substantially larger than that of the base metal. Such a precipitate distribution is typical of precipitation hardening cast alloys that have not been

subjected to a post-cast homogenization treatment. It has been described in detail for casting conditions before.^[45]

An interesting point is the hardness resulting from such microstructures. Models exist for precipitation hardening in homogeneous microstructures, and for a given precipitate size the precipitate contribution to the yield strength is proportional to the square root of the volume fraction:

$$\sigma_y^{\text{homo}} = \sigma_o + k\sqrt{f_v^{\text{homo}}}, \quad [3]$$

where k is a constant and σ_o is the strength contribution of grain boundaries and solutes. When the microstructure is heterogeneous, the situation is more complicated. A simple hypothesis can be that the precipitate volume fraction in the high solute areas is constant and equal to the volume fraction in the homogeneous case (base metal)

$$f_v^{\text{high}} = f_v^{\text{homo}} = cst \quad [4]$$

The effect of the available solute, then, is in first approximation to change the volume fraction χ of the material, where one finds the high solute content, and therefore, the average volume fraction in the heterogeneous material writes

$$f_v^{\text{hetero}} = \chi f_v^{\text{homo}} \quad [5]$$

If the yield stresses of the high and low solute regions are added by a simple rule of mixture, then the yield stress of the heterogeneous material writes

$$\sigma_y = \sigma_o + \chi k \sqrt{f_v^{\text{homo}}} = \sigma_o + \frac{f_v^{\text{hetero}}}{f_v^{\text{homo}}} k \sqrt{f_v^{\text{homo}}} = \sigma_o + k' f_v^{\text{hetero}} \quad [6]$$

Therefore, it can be expected that the contribution of precipitation hardening to the yield stress in the heterogeneous material does not scale as $f_v^{1/2}$ as in a homogeneous material, but closer to a linear relationship with f_v .

In order to apply this to our case, it is first necessary to estimate the value for σ_o . From a previous study on an alloy relatively similar to the one studied here, it was considered as about 80 MPa.^[29] The yield strength of the BM has been measured as 320 MPa.^[46] Therefore, the precipitate contribution in the BM is 240 MPa, corresponding to a precipitate volume fraction of 0.016, which results in a value for k of 1900 MPa. In the fusion zone, the precipitate volume fraction is 0.006. Thus, if the precipitate contribution to the yield strength scaled as $f_v^{1/2}$ (identical to the homogeneous case, Eq. [3]) the yield stress in the FZ would be ≈ 230 MPa. On the other hand, if the precipitate contribution to the yield strength was calculated from Eq. [6] for the heterogeneous case, the yield strength in the FZ (based on $\chi = 0.375 = 0.006/0.016$) would be 170 MPa. The experimental value has been measured by microtensile samples at 150 MPa^[46] and is very close to this second estimate. This evaluation shows that it is necessary to consider the

heterogeneous distribution of the precipitates to evaluate the resulting strength.

V. CONCLUSIONS

In this work, the main features of the 7020 aluminum alloy microstructure after EBW and two different states of post-welding heat treatment have been characterized in detail using a combination of complementary experimental techniques.

The weld consists in an assembly of the fusion zone (FZ), the heat-affected zone (HAZ), and the BM. While the grain microstructure and the distribution of intermetallic phases remain unchanged in HAZ and BM, the FZ exhibits mainly refined and isotropic grains. The electron beam process results in a solute loss of 33 pct in Zn and 18 pct in Mg. In the FZ, the solute is heterogeneously distributed following the solidification microstructure. At the center of the interdendritic, solute-rich region of the FZ, clusters of Fe-rich intermetallic nanocrystals are observed.

The spatial distribution of the hardening precipitates in the different regions of the weld assembly is intimately linked to the distribution of solute and to the thermal cycle experienced by the material during welding and during the post-welding heat treatment. The microstructure present in the heat-affected zone classically consists of different regions of precipitate dissolution, coarsening, and new precipitation after welding. After a post-welding heat treatment, the microstructure and resulting hardness distribution become relatively homogeneous throughout the HAZ. The microstructure in the FZ is, however, very heterogeneous. The precipitate density after a post-welding heat treatment follows the distribution of solute, and ranges from very high precipitate densities to completely precipitate-free regions. However, the microstructure averaged at the scale of the solidification structure is homogeneous over the whole fusion zone. The hardness resulting from the low precipitate volume fraction and heterogeneous distribution of solute is much lower than that of the base material.

Compared to microstructures resulting from more classical welding techniques, the present case is characterized by the solute loss due to the vacuum and high energy density of the electron beam, and by fast heating and cooling rate that result in a fine microstructure and in a limited coarsening of the precipitates initially present during the welding operation.

ACKNOWLEDGMENTS

The authors are very grateful to the staff of CEA Valduc for welding and metallography. Florence Robaud is thanked for the EPMA measurement; Frederic Charlot is gratefully acknowledged for his assistance on electron imaging. The staff of BM2/D2AM beamline of ESRF thanked for technical support.

REFERENCES

1. L.M. Volpone and S. Mueller: *Weld. Int.*, 2008, vol. 22, p. 597.
2. P.L. Threadgill, A.J. Leonard, H.R. Shercliff, and P.J. Withers: *Int. Mater. Rev.*, 2009, vol. 54, pp. 49–93.
3. G. Mathers: *The Welding of Aluminium and Its Alloys*, Woodhead Publishing, Cambridge, 2002.
4. A. Simar, Y. Brechet, B. de Meester, A. Denquin, C. Gallais, and T. Pardoën: *Prog. Mater. Sci.*, 2012, vol. 57, pp. 95–183.
5. T. Ma and G. den Ouden: *Mater. Sci. Eng. A*, 1999, vol. A266, pp. 198–204.
6. G.D.J. Ram, T.K. Mitra, V. Shankar, and S. Sundaresan: *J. Mater. Process. Technol.*, 2003, vol. 142, pp. 174–81.
7. A. Deschamps, G. Texier, S. Ringeval, and L. Delfaut-Durut: *Mater. Sci. Eng. A*, 2009, vol. A501, pp. 133–39.
8. F. Matsuda: *Trans. JWRI*, 1982, vol. 11, p. 87.
9. Donald.E. Powers: *Weld. J.*, 2011, vol. 90, pp. 30–34.
10. Z. Sun and R. Karppi: *J. Mater. Process. Technol.*, 1996, vol. 59, pp. 257–67.
11. P. Wanjara and M. Brochu: *Vacuum*, 2010, vol. 85, pp. 268–82.
12. B.S. Nair, S. Rakesh, G. Phanikumar, K. PrasadRao, and P.P. Sinha: *Mater. Des.*, 2010, vol. 31, pp. 4943–50.
13. D. Maisonnette, M. Suery, D. Nelias, P. Chaudet, and T. Epicier: *Mater. Sci. Eng. A*, 2011, vol. 528, pp. 2718–24.
14. G. Cam and M. Kocak: *J. Mater. Sci.*, 2007, vol. 42, pp. 7154–61.
15. A. Deschamps, S. Ringeval, G. Texier, and L. Delfaut-Durut: *Mater. Sci. Eng. A*, 2009, vol. 517, pp. 361–68.
16. J. Lendvai: *Mater. Sci. Forum*, 1996, vols. 217–222, pp. 43–56.
17. G. Waterloo, V. Hansen, J. Gjonnes, and S.R. Skjervold: *Mater. Sci. Eng. A*, 2001, vol. 303, pp. 226–33.
18. L.K. Berg, J. Gjonnes, V. Hansen, X.Z. Li, M. Knutson-Wedel, G. Waterloo, D. Schryvers, and L.R. Wallenberg: *Acta Mater.*, 2001, vol. 49, pp. 3443–51.
19. Z.H. Li, B.Q. Xiong, Y.G. Zhang, B.H. Zhu, F. Wang, and H.W. Liu: *Mater. Charact.*, 2008, vol. 59, pp. 278–82.
20. G. Fribourg, Y. Bréchet, A. Deschamps, and A. Simar: *Acta Mater.*, 2011, vol. 59, pp. 3621–35.
21. G.M. Ludka and D.E. Laughlin: *Metall. Trans. A*, 1982, vol. 13A, p. 411.
22. T. Pardoën, D. Dumont, A. Deschamps, and Y. Brechet: *J. Mech. Phys. Solids*, 2003, vol. 51, pp. 637–65.
23. Q. Puydt, S. Flouriot, S. Ringeval, F. De Geuser, R. Estevez, G. Parry, and A. Deschamps: *Metall. Mater. Trans. A*, 2014, DOI: 10.1007/s11661-014-2567-8.
24. O.R. Myhr and O. Grong: *Acta Metall. Mater.*, 1991, vol. 39, pp. 2693–2702.
25. O.R. Myhr and O. Grong: *Acta Metall. Mater.*, 1991, vol. 39, pp. 2703–08.
26. O.R. Myhr, O. Grong, H.G. Fjaer, and C.D. Marioara: *Acta Mater.*, 2004, vol. 52, pp. 4997–5008.
27. B.I. Bjorneklett, O. Grong, O.R. Myhr, and A.O. Kluken: *Metall. Mater. Trans. A*, 1999, vol. 30A, pp. 2667–77.
28. M. Nicolas and A. Deschamps: *Acta Mater.*, 2003, vol. 51, pp. 6077–94.
29. M. Nicolas and A. Deschamps: *Metall. Mater. Trans. A*, 2004, vol. 35A, pp. 1437–48.
30. S.C. Wang, F. Lefebvre, J.L. Yan, I. Sinclair, and M.J. Starink: *Mater. Sci. Eng. A*, 2006, vol. 431, pp. 123–36.
31. Reinhold. Braun: *Mater. Sci. Eng. A*, 2006, vol. 426, pp. 250–62.
32. D. Fabregue, A. Deschamps, and M. Suery: *Mater. Sci. Technol.*, 2005, vol. 21, pp. 1329–36.
33. Y.E. Wu and Y.T. Wang: *J. Mater. Eng. Perform.*, 2010, vol. 19, pp. 1362–69.
34. F. De Geuser and A. Deschamps: *C. R. Phys.*, 2012, vol. 13, pp. 246–56.
35. A. Deschamps and F. De Geuser: *Metall. Mater. Trans. A*, 2013, vol. 44A, pp. 77–86.
36. F. Zhang, J. Ilavsky, G.G. Long, J.P.G. Quintana, A.J. Allen, and P.R. Jemian: *Metall. Mater. Trans. A*, 2010, vol. 41A, pp. 1151–58.
37. A. Deschamps and F. De Geuser: *J. Appl. Crystallogr.*, 2011, vol. 44, pp. 343–52.
38. M. Dumont, W. Lefebvre, B. Doisneau-Cottignies, and A. Deschamps: *Acta Mater.*, 2005, vol. 53, pp. 2881–92.
39. P. Staron, W.V. Vaidya, and M. Kocak: *Mater. Sci. Eng. A*, 2009, vol. 525, pp. 192–99.
40. M. Dumont, A. Steuwer, A. Deschamps, M. Peel, and P.J. Withers: *Acta Mater.*, 2006, vol. 54, pp. 4793–4801.
41. C. Genevois, A. Deschamps, A. Denquin, and B. Doisneau cottignies: *Acta Mater.*, 2005, vol. 53, pp. 2447–58.
42. A. Steuwer, M. Dumont, J. Altenkirch, S. Biroasca, A. Deschamps, P.B. Prangnell, and P.J. Withers: *Acta Mater.*, 2011, vol. 59, p.3002.
43. A. Simar, Y. Brechet, B. de Meester, A. Denquin, and T. Pardoën: *Acta Mater.*, 2007, vol. 55, pp. 6133–43.
44. A. Deschamps, C. Sigli, T. Mourey, F. de Geuser, W. Lefebvre, and B. Davo: *Acta Mater.*, 2012, vol. 60, pp. 1917–28.
45. C.A. Gandin, Y. Brechet, M. Rappaz, G. Canova, M. Ashby, and H. Shercliff: *Acta Mater.*, 2002, vol. 50, pp. 901–27.
46. Q. Puydt: Ph.D. Thesis, University of Grenoble, France, 2012.